

See discussions, stats, and author profiles for this publication at: <https://www.researchgate.net/publication/263982332>

# Glass-to-Crystal Transition in $\text{Li}_{1+x}\text{Al}_x\text{Ge}_{2-x}(\text{PO}_4)_3$ : Structural Aspects Studied by Solid State

ARTICLE in THE JOURNAL OF PHYSICAL CHEMISTRY C · APRIL 2014

Impact Factor: 4.77 · DOI: 10.1021/jp502265h

CITATIONS

4

READS

71

## 4 AUTHORS, INCLUDING:



**Cornelia Schröder**

University of Münster

4 PUBLICATIONS 32 CITATIONS

SEE PROFILE



**Ana C M Rodrigues**

Universidade Federal de São Carlos

51 PUBLICATIONS 631 CITATIONS

SEE PROFILE



**Hellmut Eckert**

University of Münster

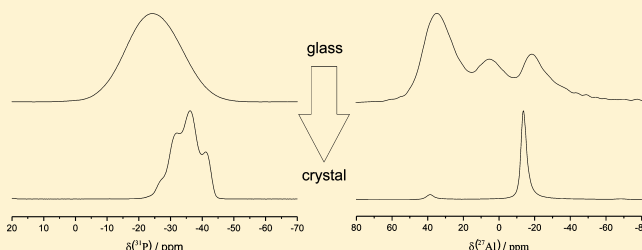
536 PUBLICATIONS 9,093 CITATIONS

SEE PROFILE

Glass-to-Crystal Transition in  $\text{Li}_{1+x}\text{Al}_x\text{Ge}_{2-x}(\text{PO}_4)_3$ : Structural Aspects Studied by Solid State NMRCornelia Schröder,<sup>†</sup> Jinjun Ren,<sup>†</sup> Ana Candida M. Rodrigues,<sup>‡</sup> and Hellmut Eckert<sup>\*,†,§</sup><sup>†</sup>Institut für Physikalische Chemie, WWU Münster, Corrensstraße 30, D 48149 Münster, Germany<sup>‡</sup>Laboratório dos Materiais Vitreos (LaMaV), Universidade Federal em São Carlos, SP Brazil<sup>§</sup>Instituto da Física em São Carlos, Universidade de São Paulo, Avenida Trabalhador Sãocarlense 400, São Carlos, SP 13590, Brazil

## S Supporting Information

**ABSTRACT:** The structural aspects of the glass-to-crystal transition in the technologically important ion conducting glass ceramic system  $\text{Li}_{1+x}\text{Al}_x\text{Ge}_{2-x}(\text{PO}_4)_3$  ( $0 \leq x \leq 0.75$ ) have been examined by complementary multinuclear solid state nuclear magnetic single and double-resonance experiments. In the crystalline state, the materials form solid solutions in the NASICON structure, with additional nanocrystalline  $\text{AlPO}_4$  present at  $x$  values  $\geq 0.5$ . Substitution of Al in the octahedral Ge sites results in a binomial distribution of multiple phosphate species, which differ in the number P–O–Al and P–O–Ge linkages and can be differentiated by  $^{31}\text{P}$  chemical shift and  $^{31}\text{P}\{^{27}\text{Al}\}$  rotational echo adiabatic passage double resonance (REAPDOR) spectroscopies. The detailed quantitative analysis of these data, of complementary  $^{27}\text{Al}\{^{31}\text{P}\}$  rotational echo double resonance (REDOR) and of homonuclear  $^{31}\text{P}$ – $^{31}\text{P}$  double quantum NMR studies suggest that the  $\text{AlO}_6$  coordination polyhedra are noticeably expanded compared to the  $\text{GeO}_6$  sites in the NASICON-type  $\text{LiGe}_2(\text{PO}_4)_3$  (LGP) structure. While the glassy state is characterized by a significantly larger degree of disorder concerning the local coordination of germanium and aluminum, dipolar solid state NMR studies clearly indicate that their medium range structure is comparable to that in NASICON, indicating the dominance of P–O–Al and P–O–Ge over P–O–P and Al–O–Ge connectivities.



## ■ INTRODUCTION

The rapid growth in global energy demand in the face of dwindling global resources has been stimulating increasing efforts toward the development of high energy and high power batteries based on both lithium ion<sup>1</sup> and solid oxide fuel cell (SOFC)<sup>2</sup> technologies. Both processes utilize fast ion transport in the solid state at ambient or elevated temperatures. During the past two decades a large number of crystalline and glassy fast ion conductors have been identified and thoroughly characterized, and excellent reviews on oxide and proton conductors for fuel cell applications,<sup>3</sup> as well as fast ion conductors for lithium batteries, are available.<sup>4–6</sup> The highest lithium ion conductivities in the solid state are generally encountered in crystalline compounds with highly disordered cation sublattices, termed *superionic crystals*. On the other hand, ion conducting glasses are often preferred in practice as they do not suffer from grain boundary effects and form more homogeneous interfaces with the anode and cathode compartments of a solid state electrochemical cell. The favorable features of both the crystalline and the glassy state can be combined in an ideal way using ion conducting glass ceramics, and numerous promising systems presenting electrical conductivities in excess of  $10^{-3} (\Omega\cdot\text{cm})^{-1}$  at room temperature have been developed.<sup>7,8</sup> One particularly attractive system is based on the crystallization of precursor glasses in the systems  $\text{Li}_2\text{O}-\text{MO}_2-\text{Al}_2\text{O}_3-\text{P}_2\text{O}_5$  ( $\text{M} = \text{Ge}, \text{Ti}$ ). While the glasses

themselves are poorly conducting, they crystallize in the NASICON structure, which features exceptionally high ionic conductivities.<sup>9–15</sup> Their structure is derived from the phases  $\text{MTi}_2(\text{PO}_4)_3$  ( $\text{M} = \text{Li}, \text{Na}$ ) and  $\text{MGe}_2(\text{PO}_4)_3$ , which feature octahedrally coordinated  $\text{Ti}^{4+}$  and  $\text{Ge}^{4+}$  cations linked through phosphate tetrahedra via corner sharing (see Figure 1).<sup>16</sup> The monovalent ions are situated within large channels and possess considerable ionic mobility. The  $\text{Ti}^{4+}$  and  $\text{Ge}^{4+}$  species can be isomorphously substituted by  $\text{Al}^{3+}$ , providing the opportunity of introducing additional monovalent cations into vacant sites of the structure. The resulting materials, having the composition  $\text{Li}_{1+x}\text{Al}_x\text{Ge}_{2-x}(\text{PO}_4)_3$  or  $\text{Li}_{1+x}\text{Al}_x\text{Ti}_{2-x}(\text{PO}_4)_3$  have shown great promise as solid electrolytes in lithium/air batteries offering potential energy densities of up to 11140 Wh/kg.<sup>17,18</sup> Further progress in this field will require a deeper fundamental understanding of the atomic structure/dynamics relationship in these electrolytes, the role of composition, the structural organization of the glassy state and the mechanism of crystallization. As previously shown, NMR spectroscopy is an element-selective, inherently quantitative method ideally well suited for developing such an understanding.<sup>19</sup> The nuclear precession frequencies are sensitively influenced by a number of

Received: March 5, 2014

Revised: April 9, 2014

Published: April 11, 2014

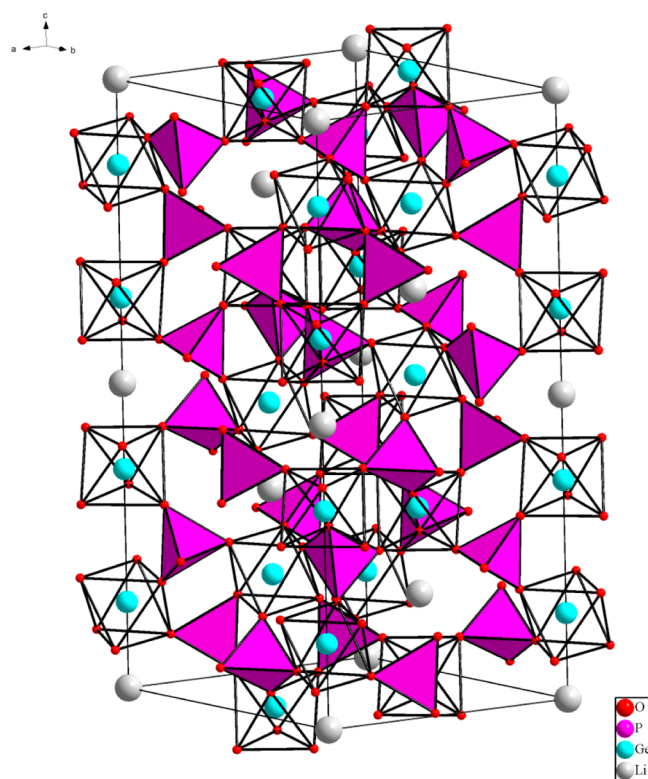


Figure 1. Crystal structure of  $\text{LiGe}_2(\text{PO}_4)_3$ .

local interactions, whose parameters reflect the details of the structural environment. Indeed, a number of solid state NMR studies have appeared in the literature, mostly on the  $\text{Li}_{1+x}\text{Al}_x\text{Ti}_{2-x}(\text{PO}_4)_3$  system, discussing the structural consequences of Al substitution, the distribution of the lithium ions over the available sites in the NASICON structure, and monitoring their mobility on the basis of Li quadrupolar splittings and spin–lattice relaxation times.<sup>20–26</sup> However, to date, no structural information is available about the local atomic environments and the polyhedral connectivities in the glassy state and the structural relation between glass and crystal. In the present contribution we address this question for the  $\text{Li}_{1+x}\text{Al}_x\text{Ge}_{2-x}(\text{PO}_4)_3$  system, which forms particularly stable glasses and glass-ceramics over a wide composition range. Besides standard magic-angle spinning (MAS) NMR we have applied a number of other selective averaging methods designed for measuring the strength of homo- and heteronuclear magnetic dipole–dipole couplings. As these interactions can be related to internuclear distance distributions, their measurement represents a powerful approach for testing spatial distribution models and interatomic connectivity scenarios in the glassy state and provides a quantitative basis for comparisons to the structures of the crystalline materials.

## MATERIALS AND METHODS

**Sample Preparation and Characterization.** Glasses were prepared from stoichiometric ratios of  $\text{Li}_2\text{CO}_3$  (Acros, 99%),  $\text{Al}_2\text{O}_3$  (Aldrich, 99.5+ %),  $\text{GeO}_2$  (Alfa Aesar, 99.98%), and  $\text{NH}_4\text{H}_2\text{PO}_4$  (Sigma-Aldrich, 99%). Starting materials were dried at 200 °C for 24 h, ground in an agate mortar, and heated at 400 °C for 2 h within a Pt crucible to decompose the ammonium dihydrogen phosphate precursor. Subsequently the mixtures were melted between 1300 and 1500 °C for approximately 1 h. Melts were rapidly quenched between two

copper or stainless steel plates. All the samples were stored inside a desiccator. Glass transition and crystallization temperatures were measured using a Netzsch STA 409 Thermal Analyzer, operated at a heating rate of 10 °C/min. The glass transition and crystallization temperatures (onset points) are listed in Table 1. Figure S1 (Supporting Information)

Table 1. Sample Compositions, Glass Transition Temperatures ( $T_g$ ), and Crystallization Temperatures ( $T_c$ )

$x$	$T_g$ (°C)	$T_c$ (°C)
0.25	555	632
0.50	521	613
0.75	489	570

summarizes the individual thermograms. Fully crystallized samples were obtained by annealing the glasses at  $T_g$  for 72 h ( $x = 0.25$ ), 700 °C for 20 min ( $x = 0.50$ ), and 670 °C for 20 min ( $x = 0.75$ ). In the latter two cases, crystallization temperatures significantly higher than  $T_g$  were necessary for obtaining fully crystalline samples within the time periods stated. The crystallized phases were characterized by X-ray powder diffraction, using a Bruker D8 Discover diffractometer. The results suggest single-phase materials, with small impurities of  $\text{Li}_4\text{P}_2\text{O}_7$  in the  $x = 0.75$  material. As discussed further below, NMR data suggest the additional presence of some nanostructured  $\text{AlPO}_4$  in the latter sample.

**Structural Investigations by Solid State NMR.** High-resolution  $^6\text{Li}$ ,  $^{27}\text{Al}$ , and  $^{31}\text{P}$  NMR spectroscopy was done under conditions of magic-angle spinning (MAS), enabling the characterization of local structural environments based on isotropic chemical shift measurements. These studies were conducted on a Bruker Avance DSX spectrometer operating at 9.4 T using a commercial 4 mm triple resonance MAS NMR probe. Typical spinning speeds between 12.0 and 14.0 kHz were used in all experiments. The spectra for  $^6\text{Li}$ ,  $^7\text{Li}$ ,  $^{27}\text{Al}$ , and  $^{31}\text{P}$  were recorded at resonance frequencies of 58.9, 155.5, 104.2, and 162.0 MHz using pulse lengths of 8.0  $\mu\text{s}$  for  $^6\text{Li}$ , 2–3.5  $\mu\text{s}$  for  $^7\text{Li}$ , 1.5–2.0  $\mu\text{s}$  for  $^{27}\text{Al}$ , and 3.0–4.0  $\mu\text{s}$  for  $^{31}\text{P}$ . Recycle delays were chosen at 60–100 s, 10 s, 0.5–1 s, and 200–1000 s for  $^6\text{Li}$ ,  $^7\text{Li}$ ,  $^{27}\text{Al}$ , and  $^{31}\text{P}$ , respectively. Resonance shifts were referenced to 1 M LiCl aqueous solution, 1 M  $\text{Al}(\text{NO}_3)_3$  aqueous solution and 85%  $\text{H}_3\text{PO}_4$ . In addition, advanced dipolar recoupling experiments were carried out to measure the strengths of hetero- and homonuclear magnetic dipole–dipole interactions under the high resolution conditions afforded by MAS. For the  $^{27}\text{Al}\{^7\text{Li}\}$ - and  $^{27}\text{Al}\{^{31}\text{P}\}$ -rotational echo double resonance (REDOR)<sup>27</sup> experiments, typical  $\pi$ -pulse lengths for  $^{27}\text{Al}$  were 6.0  $\mu\text{s}$  and 9.4  $\mu\text{s}$  for  $^7\text{Li}$  and  $^{31}\text{P}$ , respectively. The compensated REDOR method was used,<sup>28</sup> and the corrected  $^{27}\text{Al}\{^{31}\text{P}\}$ -REDOR curvatures within the data range ( $\Delta S/S_0 < 0.3$ ) were analyzed according to the parabolic approximation,<sup>29</sup>

$$\frac{\Delta S}{S_0} = \frac{4}{3\pi^2} (N \cdot T_r)^2 M_2^{\text{hetero}} \quad (1)$$

From this analysis, second moment values  $M_2(^{27}\text{Al}-^{31}\text{P})$  can be obtained characterizing the average strength of the heteronuclear dipole–dipole interactions. Such data can be compared with the van Vleck values<sup>30</sup>

$$M_2^{\text{hetero}} = \frac{4}{15} \left( \frac{\mu_0}{4\pi} \right)^2 \gamma_1^2 \gamma_S^2 \hbar^2 S(S+1) \sum_i r_i^{-6} \quad (2)$$

predicted from the relevant internuclear distances  $r_i$  involved. These distances may be available either from known crystal structure databases or they may be predicted by computational modeling/molecular dynamics simulations.

Recoupling dipolar interactions of the observed nucleus to a quadrupolar nucleus is most conveniently studied by Rotational Echo Adiabatic Passage Double Resonance (REAPDOR) experiments.<sup>31</sup> In the present contribution, these experiments employed  $\pi/2$  pulses for  $^{31}\text{P}$  of 4.4–4.6  $\mu\text{s}$  length and adiabatic passage pulses of 25.6 and 27.8  $\mu\text{s}$  (one-third of the rotor period) at the  $^{27}\text{Al}$  resonance. The experiments were conducted at a  $^{27}\text{Al}$  nutation frequency of 43.5 kHz measured on a liquid sample.

$^{27}\text{Al}$  2D-triple-quantum (TQ)-MAS NMR spectra were obtained with a three pulse z-filtering method<sup>32,33</sup> using the following acquisition parameters: 3.0  $\mu\text{s}$  and 1.2–1.6  $\mu\text{s}$  for the first two pulses at a nutation frequency of 119.0 kHz and 2.5  $\mu\text{s}$  for the last pulse at a  $^{27}\text{Al}$  nutation frequency of 41.7 kHz. Sampling in the  $t_1$  dimension was done with a dwell time of 20  $\mu\text{s}$  (1/4 rotor period). Data are presented in the sheared mode. The connectivity between and among the various aluminum species was explored by  $^{27}\text{Al}$  single quantum/double quantum correlation spectroscopy. This experiment is based on the recoupling of homonuclear  $^{27}\text{Al}$ – $^{27}\text{Al}$  dipole–dipole interactions by stimulating double quantum coherences via symmetry-based pulse sequence schemes.<sup>34</sup> In the present study, the BR2<sub>1</sub> pulse scheme developed by Wang et al.<sup>35</sup> is used for this purpose. The experiment was carried out on a Bruker DSX-400 spectrometer equipped with a 4 mm MAS probe operated at 14.0 kHz. Both the excitation and reconversion times were set to 856.7  $\mu\text{s}$ . The central transition selective  $\pi$  pulse and reading  $\pi/2$  pulse were set to 40 and 20  $\mu\text{s}$ , respectively. The rotor-synchronized increment interval in the indirect dimension  $t_1$  was set to 71.43  $\mu\text{s}$ , and the two-dimensional data sets consisted of 32 points in  $t_1$  and 512 points in  $t_2$ . 15232 and 30464 FIDs were acquired for each increment with a recycle delay of 0.2 s. The  $k$  value is set to 0.25, giving a chemical shift scaling of 0.5. Following double Fourier transformation the correlated signals are displayed at 1/2 of the sum of their chemical shifts in the F2 dimension.

Site-resolved  $^{31}\text{P}$ – $^{31}\text{P}$  homonuclear dipole–dipole coupling measurements were conducted using a recently developed dipolar recoupling method denoted DQ-DRENAR (double-quantum based dipolar recoupling effects nuclear alignment reduction).<sup>36</sup> In DQ-DRENAR, double quantum coherences are stimulated during  $2n$  rotor periods  $T_r$  using the POST-C7 excitation scheme.<sup>37</sup> This causes a decrease in the longitudinal  $^{31}\text{P}$  magnetization, which is then probed under systematic incrementation of this stimulation time. One measures a normalized difference signal  $(S_0 - S')/S_0$  by comparing the z-magnetization in the presence and the absence of the DQ-Hamiltonian, as a function of dipolar mixing time  $NT_r$ . The strength of the homonuclear multispin dipole–dipole coupling, specified by the quantity  $\sum_k b_{jk}^2$ , can then be extracted by fitting the initial data range of  $(S_0 - S')/S_0$  up to 0.3–0.5 to the expression<sup>36</sup>

$$\frac{S_0 - S'}{S_0} \Big|_{(t=NT_r)} = \frac{0.86\pi^2}{15} \left( \sqrt{\sum_k b_{jk}^2} NT_r \right)^2 \quad (3)$$

where

$$b_{jk} = \frac{\mu}{4\pi} \frac{\hbar \gamma_j^2}{2\pi r_{jk}^3} \quad (4)$$

specifies the dipolar coupling constant between the observed nucleus  $j$  and another nucleus  $k$  of the same kind, separated by the distance  $r_{jk}$ . In multispin systems, effective summed squares of dipole–dipole coupling constants can be accurately estimated by this technique. Experiments were conducted at spinning speeds of 7.0, 8.0, 9.0, 10.0, and 11.0 kHz.

## RESULTS AND DISCUSSION

**Structural Characterization of the Crystallized Materials.**  $^{31}\text{P}$  Single and Double Resonance MAS NMR. Figure 2

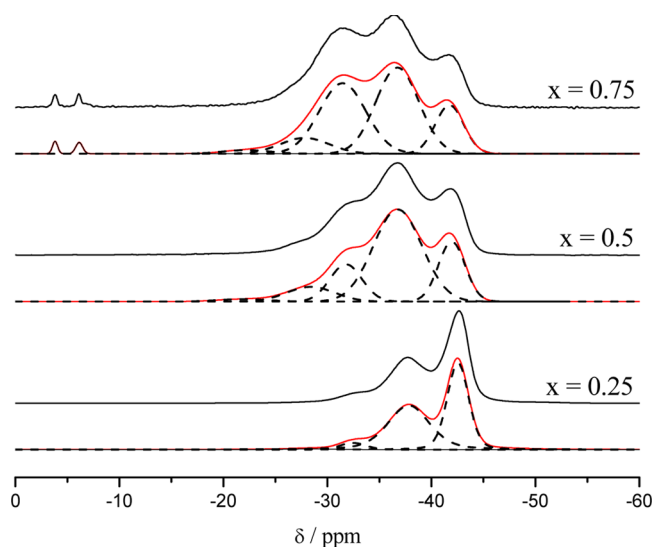


**Figure 2.**  $^{31}\text{P}$  MAS NMR spectra of crystalline  $\text{Li}_{1+x}\text{Al}_x\text{Ge}_{2-x}(\text{PO}_4)_3$  with three distinct compositions  $x$  and peak deconvolutions into five Gaussian components.

shows the  $^{31}\text{P}$  MAS NMR spectra of crystalline  $\text{Li}_{1+x}\text{Al}_x\text{Ge}_{2-x}(\text{PO}_4)_3$  with three distinct compositions  $x$ . The spectra are consistent with the XRD results, suggesting the formation of single-phase materials and small amounts of  $\text{Li}_4\text{P}_2\text{O}_7$  for the  $x = 0.75$  composition. In the region between  $-20$  and  $-40$  ppm, multiple signals are observed, whose intensity distribution depends on the aluminum content. The individual peaks are assigned to the five possible phosphorus environments,  $\text{P}^{(4)}_{n\text{Al}}$  ( $0 \leq n \leq 4$ ), differing in the number  $n$  of Al next nearest neighbors. From the compositional dependence it is clear that the  $^{31}\text{P}$  chemical shift increases with increasing number of Al atoms in the second coordination sphere of phosphorus. While the analogous assignment was proposed previously for samples in the Ti-based system,<sup>21</sup> the spectroscopic resolution is significantly better in the present case and is comparable to that observed in NASICON-type  $\text{Na}_{1+x}\text{Zr}_{2-x}\text{In}_x(\text{PO}_4)_3$ .<sup>38</sup> The intensity ratios follow binomial statistics, consistent with random substitution of Ge by Al in the octahedral sites. Table 2 summarizes the peak deconvolutions, from which the Al/Ge ratio of the crystals can be back-calculated, using the formula<sup>21,41</sup>

$$\frac{\text{Al}^{3+}}{\text{Ge}^{4+}} = \frac{4I_4 + 3I_3 + 2I_2 + I_1}{I_3 + 2I_2 + 3I_1 + 4I_0} = \frac{x}{2-x} \quad (5)$$



**Table 2. Structural Units, Chemical Shifts ( $\pm 0.2$  ppm), and Fractional Areas ( $\pm 0.5\%$ ) of the Various  $^{31}\text{P}$  Species Observed in Crystalline  $\text{Li}_{1+x}\text{Al}_x\text{Ge}_{2-x}(\text{PO}_4)_3$ <sup>a</sup>**

$x$	unit	$\delta$ (ppm)	area (%)
0.25 (0.29)	$\text{P}^{(4)}_{3\text{Al}}$	-27.8	0.5
	$\text{P}^{(4)}_{2\text{Al}}$	-32.3	3.8
	$\text{P}^{(4)}_{1\text{Al}}$	-37.8	49.5
	$\text{P}^{(4)}_{0\text{Al}}$	-42.5	46.2
0.50 (0.58)	$\text{P}^{(4)}_{4\text{Al}}$	-23.3	1.0
	$\text{P}^{(4)}_{3\text{Al}}$	-27.0	6.4
	$\text{P}^{(4)}_{2\text{Al}}$	-31.3	26.5
	$\text{P}^{(4)}_{1\text{Al}}$	-36.3	51.5
	$\text{P}^{(4)}_{0\text{Al}}$	-41.5	14.6
0.75 (0.66)		-3.8 ( $\text{Li}_4\text{P}_2\text{O}_7$ )	0.7
		-6.1 ( $\text{Li}_4\text{P}_2\text{O}_7$ )	0.8
	$\text{P}^{(4)}_{4\text{Al}}$	-22.2	1.7
	$\text{P}^{(4)}_{3\text{Al}} + \text{AlPO}_4$	-27.8	8.2
	$\text{P}^{(4)}_{2\text{Al}}$	-31.5	34.7
	$\text{P}^{(4)}_{1\text{Al}}$	-36.7	39.2
	$\text{P}^{(4)}_{0\text{Al}}$	-41.7	14.7

<sup>a</sup> $x$ -Values listed in parentheses are calculated compositions based on the peak area analysis using eq 5.

Table 2 illustrates reasonable agreement between nominal and derived sample compositions. Enhanced Al concentrations have been observed, however, for samples prepared within alumina crucibles (data not shown). In the case of the  $x = 0.75$  sample, application of eq 5 to the peak areas listed in Table 2 would result in an  $x$ -value of 0.71. However, based on the  $^{27}\text{Al}$  NMR results discussed below, 6% of the phosphorus inventory is concluded to be present in the form of  $\text{AlPO}_4$  and will thus contribute to the  $^{31}\text{P}$  NMR signal component near -28.0 ppm. Taking this effect into consideration, the correct composition of the NASICON phase is deduced to be  $x = 0.66$ . The peak assignments summarized in Table 2 are independently confirmed using  $^{31}\text{P}\{^{27}\text{Al}\}$  REAPDOR NMR. Figure 3b illustrates the difference in dipolar dephasing observed for the various components of the  $^{31}\text{P}$  MAS NMR line shape, indicating that the  $^{27}\text{Al}$ - $^{31}\text{P}$  dipole-dipole coupling strength increases with increasing chemical shift. Figure 3b shows a quantitative comparison of the experimental REAPDOR

dephasing curves observed for the different line shape components with simulations for various  $\text{PAl}_n$  spin cluster systems using the SIMPSON software.<sup>39</sup> These simulations take into consideration the experimental  $^{27}\text{Al}$  nuclear electric quadrupolar coupling constant of 1.8 MHz (see results below), a  $\text{P}\cdots\text{Al}$  internuclear distance of 3.10 Å, using the value from the LGP crystal structure, and the experimental  $^{27}\text{Al}$  nutation frequency used in the REAPDOR experiment. The resonance near -41 ppm shows a near-zero REAPDOR effect, thus justifying its assignment to a  $\text{P}^{(4)}_{4\text{Ge}}$  unit. The REAPDOR curve observed for the -36 ppm resonance agrees rather well with that simulated for a  $^{31}\text{P}\cdots^{27}\text{Al}$  two-spin system, in accordance with its assignment to a  $\text{P}^{(4)}_{3\text{Ge}1\text{Al}}$  unit. For the -31 ppm peak the agreement of the experimental data with that predicted for a  $\text{P}^{(4)}_{2\text{Ge}2\text{Al}}$  unit is only qualitative and this suggests that the  $\text{P}\cdots\text{Al}$  distances are actually somewhat larger than those present in the LGP structure. As indicated below, this conclusion is consistent with results from  $^{27}\text{Al}\{^{31}\text{P}\}$  REDOR and  $^{31}\text{P}$ -DQ-DRENAR experiments. Finally, Figure 3 indicates that the REAPDOR curves measured for the  $\text{P}^{(4)}_{1\text{Ge}3\text{Al}}$  and  $\text{P}^{(4)}_{0\text{Ge}4\text{Al}}$  units are not consistent with their assignments. However, we have to bear in mind that the limited peak intensities observed for these higher-frequency peaks make the REAPDOR analysis difficult, which may result in large experimental errors.

The strength of the homonuclear  $^{31}\text{P}$ - $^{31}\text{P}$  magnetic dipole-dipole interactions was studied in a site-resolved fashion on the  $x = 0.5$  sample using the above-described DQ-DRENAR method. The results are summarized in Figure 4. The average squared dipolar coupling constants  $\sum_k b_{jk}^2$  obtained from the parabolic analysis (eq 3) from these individual DRENAR curves within the data range  $\Delta S/S_0 < 0.5$  are summarized in Table 3. They may be compared to the value of  $6.6 \cdot 10^5 \text{ Hz}^2$  calculated from the crystal structure of LGP, where the shortest  $\text{P}\cdots\text{P}$  distance is 4.12 Å. There is a clear trend toward a decreased  $^{31}\text{P}$ - $^{31}\text{P}$  dipole-dipole coupling strength in the Al-substituted material, with a successive weakening of the interaction relative to that found for the  $\text{P}^{(4)}_{4\text{Ge}}$  site, for those  $\text{P}^{(4)}$  sites with increasing numbers of Al in the second coordination sphere. These results suggest that local substitution of a  $\text{Ge}^{4+}$  ion by an  $\text{Al}^{3+}$  ion results in an expansion of the octahedral site. The decrease of  $\sum_k b_{jk}^2$  from  $6.6 \times 10^5 \text{ Hz}^2$  for the  $\text{P}^{(4)}_{4\text{Ge}}$  site in LGP to  $4.4 \times 10^5 \text{ Hz}^2$  for the  $\text{P}^{(4)}_{4\text{Al}}$  site in the Al-substituted

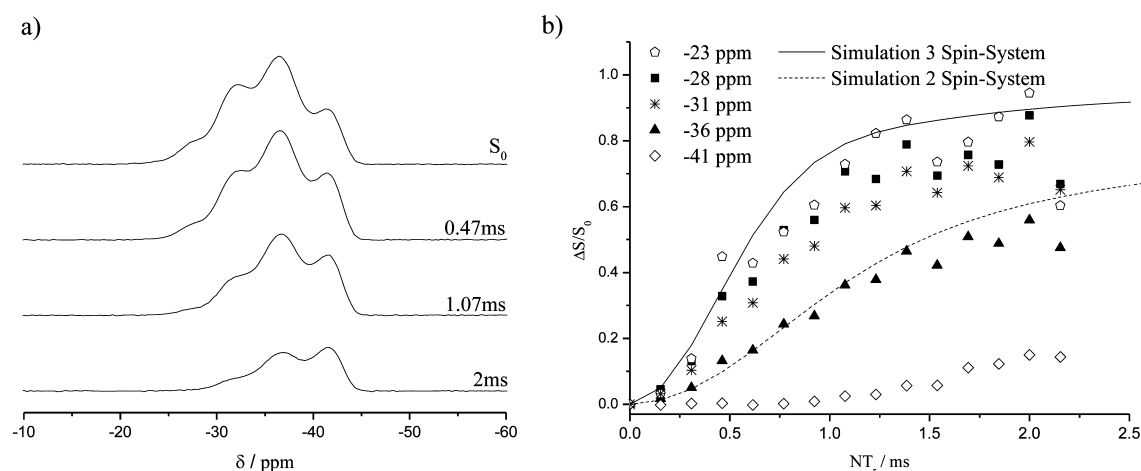


**Figure 3.**  $^{31}\text{P}\{^{27}\text{Al}\}$  REAPDOR data of a crystalline sample with the nominal composition  $\text{Li}_{1.5}\text{Al}_{0.5}\text{Ge}_{1.5}(\text{PO}_4)_3$ . (a) Fourier Transforms of  $^{31}\text{P}$  spin echoes without recoupling ( $S_0$ ) and with  $^{27}\text{Al}$  recoupling for mixing times of 0.47, 1.07, and 2.0 ms, respectively. (b) Site-resolved comparison of the experimental data with simulated curves for two- and three-spin systems, assuming a  $\text{P}\cdots\text{Al}$  internuclear distance of 3.10 Å.

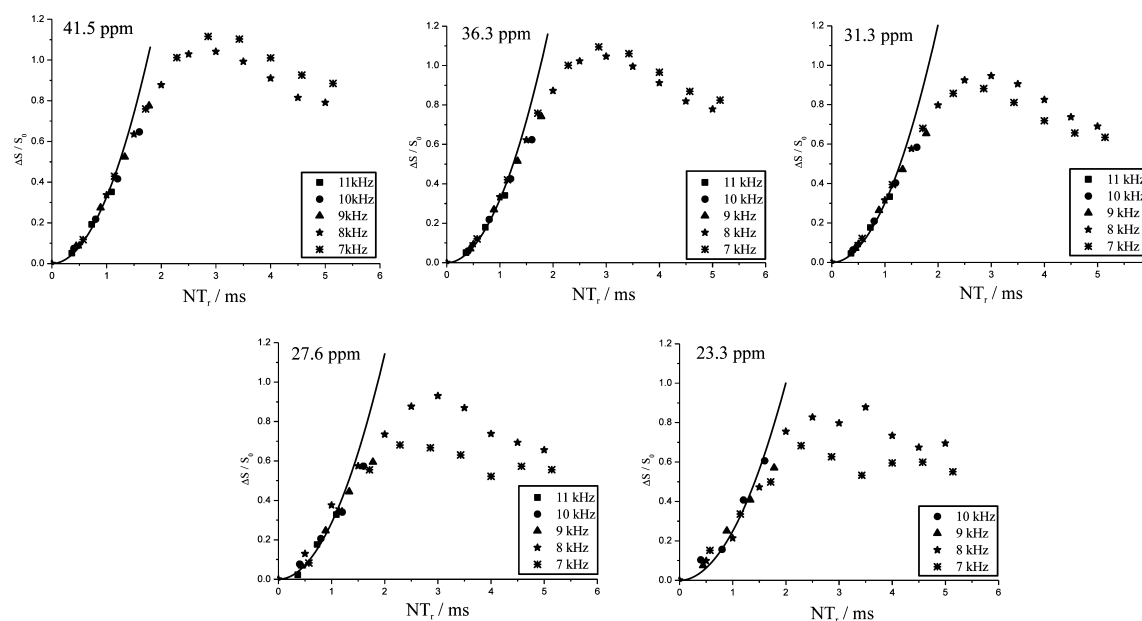


**Figure 4.** Individual DRENAR curves associated with the five resolved  $^{31}\text{P}$  resonances in a crystalline sample with nominal composition  $\text{Li}_{1.5}\text{Al}_{0.5}\text{Ge}_{1.5}(\text{PO}_4)_3$ , corresponding to the various  $\text{P}^{(4)}_{\text{nAl}}$  sites. To acquire enough data points for the initial rate analysis, data were measured at different MAS rotation frequencies.

**Table 3.** Average Summed Squared Dipolar Coupling Constants  $\sum_k b_{jk}^2$  Extracted from the Individual DRENAR Curves Associated with the Five Resolved  $^{31}\text{P}$  Resonances in Crystalline  $\text{Li}_{1.5}\text{Al}_{0.5}\text{Ge}_{1.5}(\text{PO}_4)_3$

$\delta_{\text{iso}}$ (ppm)	site	$\sum b_{jk}^2$ ( $10^5 \text{ Hz}^2$ )
−41.5	$\text{P}^{(4)}_{4\text{Ge0Al}}$	5.8
−36.3	$\text{P}^{(4)}_{3\text{Ge1Al}}$	5.7
−31.3	$\text{P}^{(4)}_{2\text{Ge2Al}}$	5.3
−27.6	$\text{P}^{(4)}_{1\text{Ge3Al}}$	5.0
−23.3	$\text{P}^{(4)}_{0\text{Ge4Al}}$	4.4

material corresponds to an average lengthening of the  $\text{P}\cdots\text{P}$  distance by 7%. These results are in good quantitative agreement with the  $^{27}\text{Al}\{^{31}\text{P}\}$  REDOR data to be discussed below.

**$^{27}\text{Al}$  Single and Double Resonance MAS NMR.** Figure 5 summarizes the  $^{27}\text{Al}$  MAS NMR spectra. The interaction parameters extracted from additional TQMAS experiments (data shown in Figure S2 of the Supporting Information) are summarized in Table 4. For all three compositions the dominant resonance at an isotropic chemical shift near −13 ppm corresponds to the expected  $^{27}\text{Al}$  NMR signal of the six-coordinated aluminum site. In addition, Figure 5 indicates the appearance of a new signal ( $\delta_{\text{iso}} \sim 39$  ppm) for the  $x = 0.5$  and 0.75 samples, signifying aluminum in a four-coordinate environment.

$^{27}\text{Al}\{^{31}\text{P}\}$  REDOR data are summarized in Figure 6, indicating that the second coordination sphere of both aluminum species is dominated by phosphorus. Data analysis within the range  $\Delta S/S_0 < 0.3$  according to eq 1 yields second moment values  $M_2 = 4.6 \times 10^6 \text{ rad}^2/\text{s}^2$  and  $6.8 \times 10^6 \text{ rad}^2/\text{s}^2$  for the six-coordinated Al species in the  $x = 0.5$  and the  $x = 0.75$  samples, respectively. These values are to be compared with a value of  $7.4 \times 10^6 \text{ rad}^2/\text{s}^2$  computed from the crystal structure of LGP, assuming the  $\text{P}\cdots\text{Al}$  distance to be identical to the  $\text{P}\cdots\text{Ge}$  distance in the latter compound. While the agreement for the  $x = 0.75$  sample can be considered within the usual

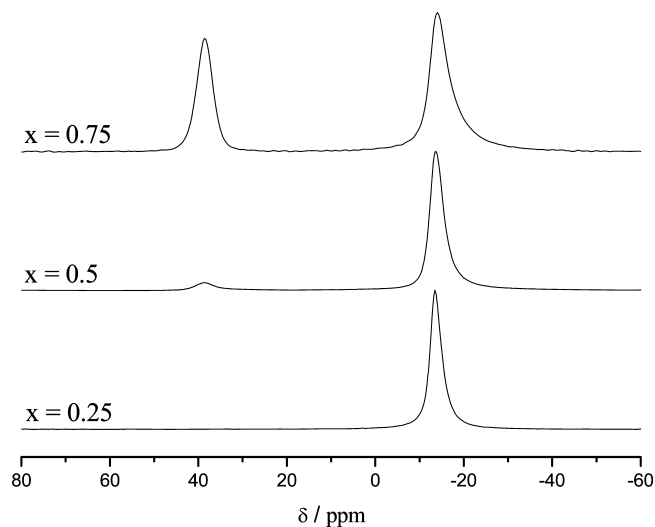


**Figure 5.**  $^{27}\text{Al}$  MAS NMR spectra of crystalline  $\text{Li}_{1+x}\text{Al}_x\text{Ge}_{2-x}(\text{PO}_4)_3$  with three distinct compositions  $x$ .

experimental error of  $\pm 10\%$  the deviation observed for the  $x = 0.5$  sample may indicate that the  $\text{P}\cdots\text{Al}$  distances are somewhat enlarged locally. From the experimental  $M_2$  value a distance of 3.30 Å can be deduced, corresponding to a lengthening of the  $\text{Al}\cdots\text{P}$  distance by  $\sim 7\%$  compared to the  $\text{Ge}\cdots\text{P}$  distance.

This conclusion is qualitatively consistent with the  $^{31}\text{P}\{^{27}\text{Al}\}$  REAPDOR and  $^{31}\text{P}$  DQ-DRENAR results detailed above. The appearance of a four-coordinated Al environment noted for both the  $x = 0.5$  and 0.75 samples has been subject to considerable discussion in the literature, relating to analogous observations in the Ti-based system.<sup>21–24</sup> It indicates that, besides the isomorphous Al for Ge substitution, a second process occurs during the crystallization, which gains importance with increasing Al content. Crystallization of additional  $\text{AlPO}_4$  has been invoked, assuming a decomposition process according to

**Table 4. Solid State  $^{27}\text{Al}$  NMR Lineshape Parameters Extracted for the Individual Aluminum Coordination States from TQMAS-NMR Data Obtained on Glassy  $\text{Li}_{1+x}\text{Al}_x\text{Ge}_{2-x}(\text{PO}_4)_3$  Samples with Three Distinct Compositions  $x^a$**

$x$	coordination number	$\delta_{\text{iso}}$ (ppm $\pm$ 0.5)	SOQE/MHz $\pm$ 0.2 <sup>b</sup>
0.75	4	41.2 (38.3)	3.3 (0.5)
	5	11.2	3.0
	6	−14.2 (−13.4)	2.5 (1.2)
0.5	4	41.6 (39.0)	3.2 (1.0)
	5	10.5	3.1
	6	−14.4 (−13.2)	2.6 (1.8)
0.25	4	43.4 (39.1)	4.1 (1.3)
	5	10.0	3.4
	6	−15.2 (−13.2)	2.9 (1.0)

<sup>a</sup>Data for the crystallized samples are given in parentheses. <sup>b</sup>SOQE = second order quadrupole effect =  $C_Q(1 + \eta^2/3)^{1/2}$ .

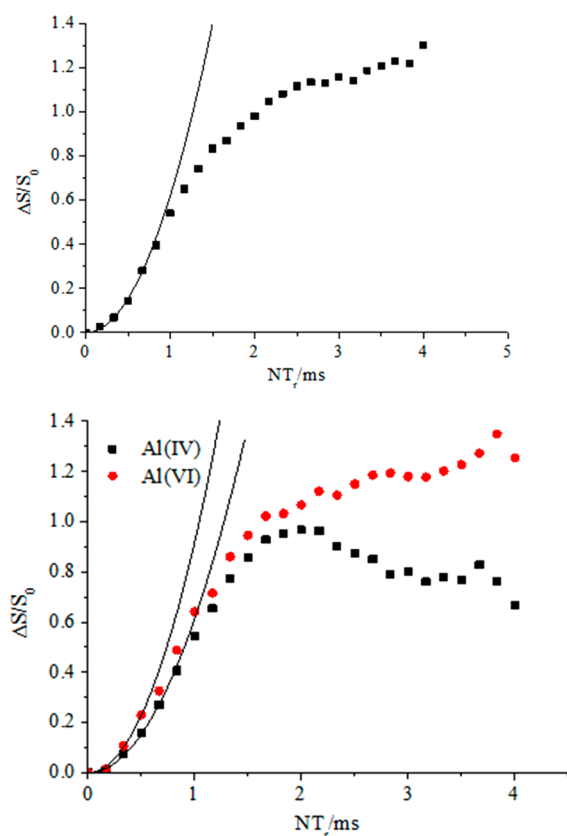
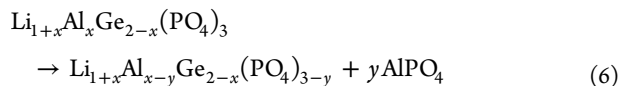


**Figure 6.**  $^{27}\text{Al}\{^{31}\text{P}\}$  REDOR curves measured for (top) the  $\text{Al}^{(6)}$  signal in a crystallized sample with the nominal composition  $\text{Li}_{1.5}\text{Al}_{0.5}\text{Ge}_{1.5}(\text{PO}_4)_3$ , and (bottom) the  $\text{Al}^{(4)}$  and  $\text{Al}^{(6)}$  signals in a crystallized sample with the nominal composition  $\text{Li}_{1.75}\text{Al}_{0.75}\text{Ge}_{1.25}(\text{PO}_4)_3$ . The solid curves are parabolic fits (according to eq 1) to the experimental data points within the range  $\Delta S/S_0 < 0.3$ .



This explanation is plausible particularly in view of the fact that the  $^{27}\text{Al}$  chemical shift is identical to the one measured in crystalline  $\text{AlPO}_4$  (berlinite). From the integration of the  $^{27}\text{Al}$  NMR signal,  $y$  can be estimated as 0.03 and 0.18, for the  $x = 0.5$  and the  $x = 0.75$  materials, respectively. In the latter case, the

mass fraction of the  $\text{AlPO}_4$  in the crystallized materials would be near 10%, that is, somewhat above the generally accepted detection limit of powder diffractometry if the phase is well crystallized. On the other hand, the XRD powder pattern of the  $x = 0.75$  phase obtained in the present study (Figure S2) shows no evidence of secondary phase formation. Of course minor fractions of  $\text{AlPO}_4$  impurities may easily escape XRD detection if they are nanocrystalline. Alternatively, Forsyth et al. and subsequently also Losilla and co-workers have attributed their observation of four-coordinate aluminum to a partial substitution of phosphate species by  $\text{AlO}_4^-$  units in the anionic sublattice.<sup>23,24</sup> In this case, the formation of a separate lithium phosphate phase would be expected. Indeed, Figure 1 confirms the formation of crystalline  $\text{Li}_4\text{P}_2\text{O}_7$ , which was also observed by X-ray powder diffraction. Furthermore, if both the four- and the six-coordinated Al species occur within the same phase, a magnetic dipole–dipole interaction between them should be detectable, for example via the excitation of a  $^{27}\text{Al}$  double quantum coherence. This concept was recently demonstrated experimentally in a  $\text{LaAlO}_3$  glassy material.<sup>40</sup> A 2-D single quantum/double quantum correlation experiment obtained with this particular objective (Figure S3) shows only diagonal peaks, however, revealing DQ coherence buildup due to dipolar coupling among equivalent four-coordinated Al species and dipolar coupling among equivalent six-coordinated Al species. No cross-peaks correlating the four- and the six-coordinated aluminum species were detectable, however, giving no positive evidence for the Forsyth model. Likewise, the  $^{31}\text{P}\{^{27}\text{Al}\}$  CP/HETCOR spectrum (see Figure S4) is more consistent with a separate  $\text{AlPO}_4$  phase, as the  $^{27}\text{Al}$  resonance near 39 ppm is found to be exclusively correlated with a signal at  $\delta_{\text{iso}}(^{31}\text{P}) = -28.0$  ppm (chemical shift of  $\text{AlPO}_4$ -berlinite) and no other  $^{31}\text{P}$  resonances. A decisive distinction between the two models is given by the  $^{27}\text{Al}\{^{31}\text{P}\}$  REDOR data shown in Figure 6b, for the  $\text{Al}^{(4)}$  signal. The experimental second moment of  $4.6 \times 10^6 \text{ rad}^2 \text{ s}^{-2}$  is close to that measured experimentally ( $4.8 \times 10^6 \text{ rad}^2 \text{ s}^{-2}$ ) for the berlinite polymorph of  $\text{AlPO}_4$ . While the theoretically expected value for berlinite is  $6.2 \times 10^6 \text{ rad}^2 \text{ s}^{-2}$  systematic deviations between experimental and theoretical values of this magnitude are rather common. A review of other  $\text{AlPO}_4$  polymorphs reveals  $M_2(^{31}\text{P}-^{27}\text{Al})$  values within a range of  $5.8\text{--}6.2 \times 10^6 \text{ rad}^2 \text{ s}^{-2}$ . In contrast, the  $\text{AlO}_4^-$  for  $\text{PO}_4^{3-}$  substitution model predicts much longer  $^{27}\text{Al}\cdots^{31}\text{P}$  internuclear distances (4.12 Å) and, hence a substantially smaller  $M_2$  value of  $2.1 \times 10^6 \text{ rad}^2 \text{ s}^{-2}$ , which is clearly at variance with the experimental data. We can therefore conclude that the dominant side reaction observed at higher  $x$  values corresponds to process 6. For the nominal  $x = 0.75$  sample, the number  $y = 0.18$  implies that the actual extent of Al substitution corresponds to only  $x = 0.57$ . We consider this the lower limit, as a minor fraction of Al might indeed substitute on the phosphate sites. As discussed above, from an analysis of the  $^{31}\text{P}$  MAS NMR spectrum we deduce  $x = 0.66$ , by correcting for the fact that  $\text{AlPO}_4$  contributes to the line shape component attributed to the  $\text{Q}^{(4)}_{3\text{Al}}$  sites near  $-28$  ppm. The quantitative contribution is  $0.18/3 = 6\%$  of the total  $^{31}\text{P}$  NMR area.

**$^7\text{Li}$  and  $^6\text{Li}$  MAS NMR.** Figure 7, top, shows the  $^7\text{Li}$  MAS NMR spectra obtained at room temperature. The Lorentzian lineshapes and the very low spinning sideband intensities indicate that the large majority of the lithium species are in the fast motion limit. Thus, the spectra only reflect the time-averaged chemical environment. There is a strong dependence of the isotropic chemical shifts on  $x$ : averaged chemical shifts

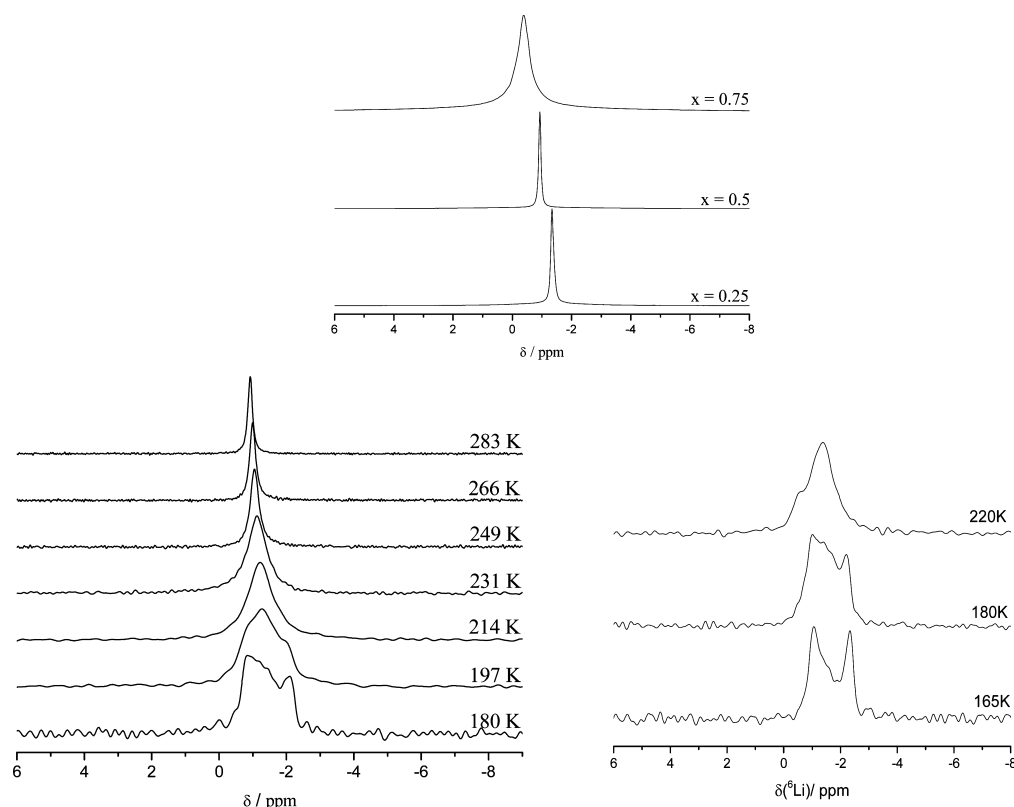


**Figure 7.** Top,  ${}^7\text{Li}$  MAS NMR spectra of crystalline  $\text{Li}_{1+x}\text{Al}_x\text{Ge}_{2-x}(\text{PO}_4)_3$  with three distinct compositions  $x$ . Bottom, variable temperature  ${}^6\text{Li}$  MAS NMR spectra of crystalline samples with nominal compositions  $\text{Li}_{1.5}\text{Al}_{0.5}\text{Ge}_{1.5}(\text{PO}_4)_3$  (left) and  $\text{Li}_{1.75}\text{Al}_{0.75}\text{Ge}_{1.25}(\text{PO}_4)_3$  (right).

are  $-1.3$ ,  $-1.0$ , and  $-0.4$  ppm for  $x = 0.25$ ,  $0.50$ , and  $0.75$ , respectively. This is not unexpected because the crystallographic Li site in LGP is fully occupied and the substitution of Ge by Al + Li leads to the additional introduction of lithium, which increases the occupancy of the interstitial Li2 site (which is vacant in LGP), as  $x$  is increased. Thus, the shift trend reflects an increasing contribution of the Li2 site to the averaged lithium environment as  $x$  is increased. Figure 7, bottom, shows low-temperature  ${}^6\text{Li}$  MAS NMR spectra obtained on the  $x = 0.50$  and  $0.75$  samples in an attempt to freeze out the lithium ion diffusion on the NMR time scale. (The  ${}^6\text{Li}$  isotope was chosen here to reduce homonuclear dipolar broadening effects, which still affect the MAS NMR spectra of the more abundant, higher-gamma  ${}^7\text{Li}$  isotope, resulting in improved spectroscopic resolution).<sup>41</sup> Indeed, at  $165$  K, the lowest temperature accessible, the data obtained for the  $x = 0.75$  sample indicate almost complete separation into the two distinct lithium sites. Based on the composition dependence of the spectra shown in the fast exchange limit, we assign the peak observed at  $-2.1$  ppm the regular LGP site Li1, and the peak at  $-0.9$  ppm to the lithium ions Li2 on the interstitial sites. At  $180$  K and above, part of the lithium ions still seem to be undergoing exchange on the NMR time scale, producing considerable additional spectral intensity in the in-between frequency region. The simultaneous occurrence of lithium species in the slow- and in the fast-exchange regime apparent near  $180$  K suggests some dynamical heterogeneity, corresponding to a distribution of lithium ionic mobilities. At temperatures above  $200$  K, we observe the successive transition into the intermediate- and fast-exchange regions. This exchange narrowing is accompanied by a gradual increase of  $\delta_{\text{iso}}({}^6\text{Li})$  with increasing temperature, reflecting the

generally positive temperature coefficient of the lithium NMR chemical shifts.

**Structural Characterization of the Glassy State.**  ${}^{31}\text{P}$  Single and Double Resonance MAS NMR. Figure 8 summarizes the  ${}^{31}\text{P}$  MAS NMR data measured for the glass samples. Broad Gaussian-shaped curves are obtained, whose central chemical shifts move from  $-23.5$  ppm ( $x = 0.25$ ) to  $-24.7$  ppm ( $x = 0.50$ ) to  $-28.3$  ppm ( $x = 0.75$ ). The chemical shifts observed in the glasses occur at significantly higher values than the centers of gravity of the peak multiplets measured in

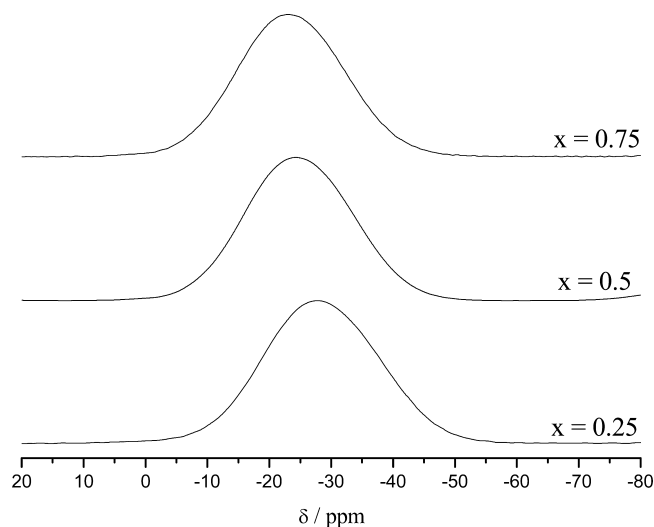


**Figure 8.**  ${}^{31}\text{P}$  MAS NMR spectra of glassy  $\text{Li}_{1+x}\text{Al}_x\text{Ge}_{2-x}(\text{PO}_4)_3$  with three distinct compositions  $x$ .



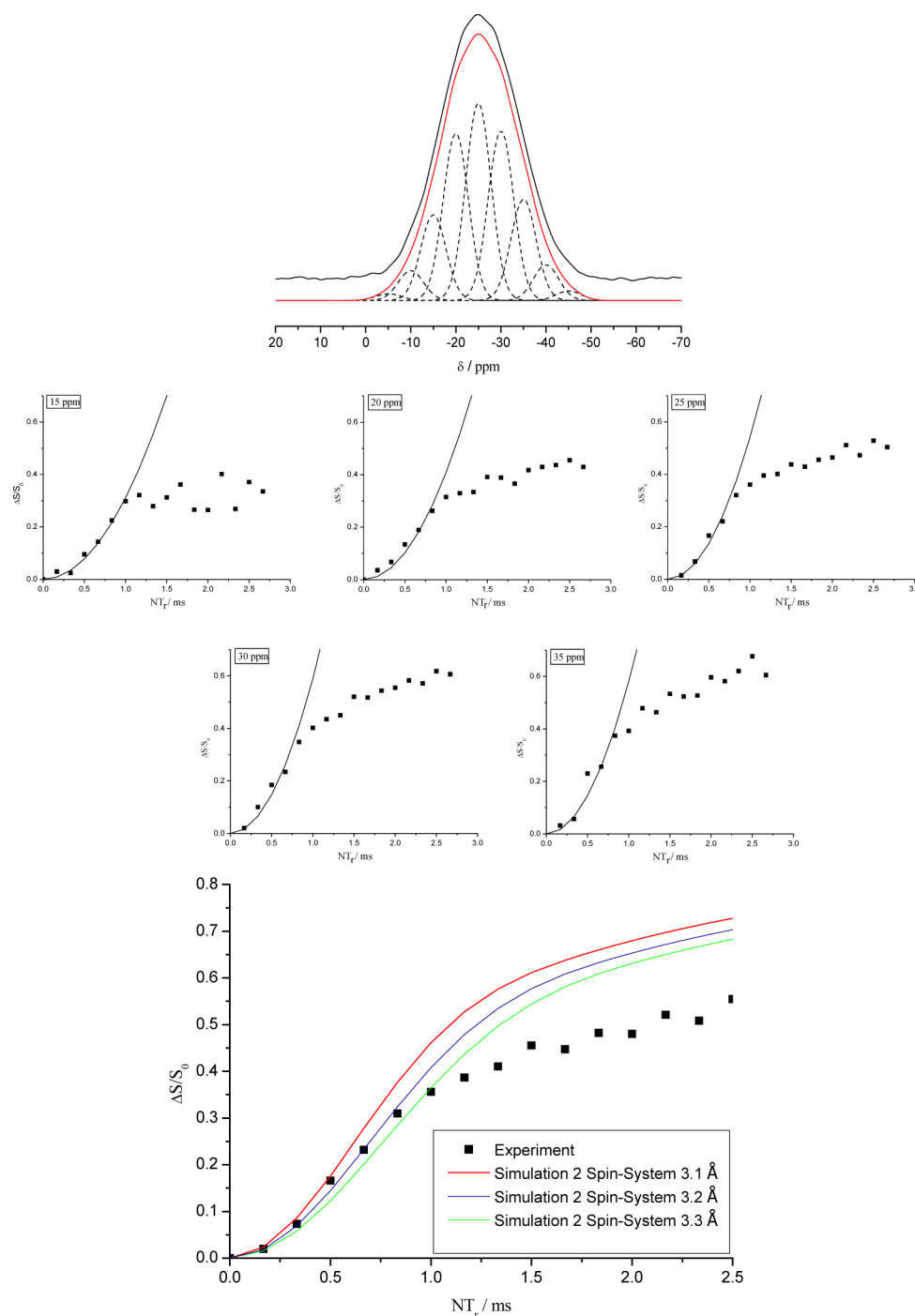


**Figure 9.**  $^{31}\text{P}/^{27}\text{Al}$  dipolar coupling in glassy  $\text{Li}_{1.5}\text{Al}_{0.5}\text{Ge}_{1.5}(\text{PO}_4)_3$ . Top: artificial deconvolution of the  $^{31}\text{P}$  MAS NMR line shape in terms of nine equally spaced components. Middle: frequency-selected  $^{31}\text{P}\{^{27}\text{Al}\}$  REAPDOR data analysis based on this line shape deconvolution. The curvatures of the parabolic fits are indicated. Bottom:  $^{31}\text{P}\{^{27}\text{Al}\}$  REAPDOR data obtained for the whole line shape without deconvolution. Data are compared with simulations based on  $^{31}\text{P}\cdots^{27}\text{Al}$  two-spin systems with internuclear distances of 3.10, 3.20, and 3.30 Å.

the crystalline compounds. This shift indicates that the structural organization of these glasses differs substantially from those in the crystals in this respect. The full width at half-maximum remains approximately constant near  $3300 \pm 100$  Hz, reflecting a distribution of isotropic chemical shifts caused by variations in the local environments of the phosphate ions.

To explore whether this chemical shift dispersion is associated with a variation of the number of Al atoms in the second coordination sphere of the phosphate ions, an  $^{31}\text{P}\{^{27}\text{Al}\}$  REAPDOR experiment was carried out and analyzed by

deconvoluting the MAS NMR line shape into nine Gaussian components of equal width and an equal frequency spacing of 5 ppm (see Figure 9a). The results of this analysis are summarized in Figure 9b for those five central components (−15 to −35 ppm) for which the signal-to-noise ratio allowed a meaningful data analysis. The curvatures of the parabolaes are seen to increase steadily with decreasing resonance frequency, from  $0.31 \text{ ms}^{-2}$  for the −15 ppm component, toward  $0.59 \text{ ms}^{-2}$  (for the −30 and −35 ppm components), suggesting that also in the glass the strength of the  $^{31}\text{P}$ – $^{27}\text{Al}$  magnetic dipole–

dipole coupling is correlated with the  $^{31}\text{P}$  isotropic chemical shifts. Interestingly, however, the correlation is opposite to that observed in the crystalline state: lower chemical shifts are associated with stronger  $^{27}\text{Al}$ – $^{31}\text{P}$  dipolar interaction strength. Thus, we must conclude that the  $^{31}\text{P}$  chemical shifts in the glassy state are dominated by other effects than simply the Al/Ge distribution in the neighboring six-coordinate sites. This can also be rationalized by the  $^{27}\text{Al}$  MAS NMR spectra (to be discussed below), which show aluminum in four-, five-, and six-coordination. We suspect that germanium likewise is not fully six-coordinated in the glassy state but also occurs in coordination numbers five and four. This view is supported by  $^{29}\text{Si}$  NMR spectra obtained on alkali phosphosilicate glasses featuring comparable alkali/silicon/phosphorus molar ratios.<sup>42</sup> Such glasses contain both four- and six-coordinate silicon, whose second coordination sphere is dominated by phosphorus.<sup>43</sup> Figure 9c illustrates that the overall  $^{31}\text{P}\{^{27}\text{Al}\}$  REDOR curve measured for the  $x = 0.5$  sample agrees well with a simulation based on a single aluminum neighbor at an internuclear distance of  $3.20 \pm 0.10$  Å. This value corresponds to the average environment of the phosphate species in a glass having a germanium to aluminum ratio of 3:1 if the Al–O–P versus the Ge–O–P connectivity distribution is random. The parabolic curvature determined for the REDOR analysis of the overall line shape is  $0.49 \text{ ms}^{-2}$  (Figure 9c). Taking this value as representative for P atoms with a single P–O–Al linkage, we conclude that the high-frequency wing of the  $^{31}\text{P}$  MAS peak in Figure 9a represents P atoms with a lower average P–O–Al connectivity, while the low-frequency wing represents P atoms with a higher average P–O–Al connectivity.

Further insights can be obtained by the DQ-DRENAR experiment shown in Figure 10. The average value of  $\sum_k b_{jk}^2 =$

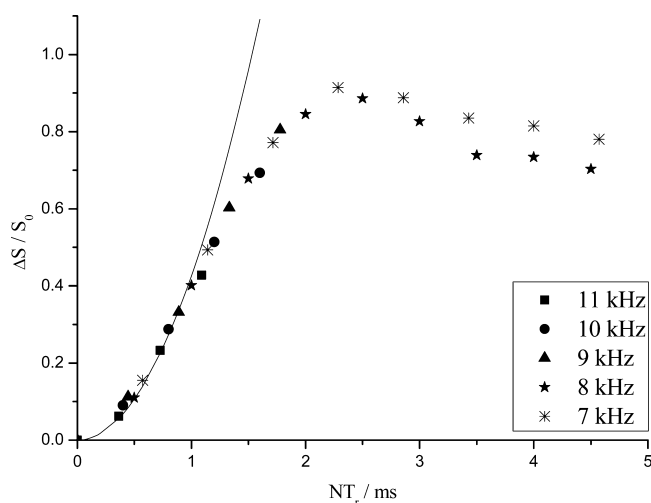


**Figure 10.**  $^{31}\text{P}$  DQ-DRENAR curve of glass with the nominal composition  $\text{Li}_{1.5}\text{Al}_{0.5}\text{Ge}_{1.5}(\text{PO}_4)_3$ . The solid curve is a parabolic fit to the experimental data points within the data range  $\Delta S/S_0 < 0.4$ .

$7.5 \times 10^5 \text{ Hz}^2$  is significantly larger than that measured in the crystalline compound, suggesting, on average, a stronger  $^{31}\text{P}$ – $^{31}\text{P}$  magnetic dipole–dipole coupling strengths in the glassy state. This finding appears plausible, as the crystal structure of LGP corresponds to an ordering scheme with a maximized dispersion of the phosphate ions, leading to the highest possible phosphorus–phosphorus separation at the composition given. In the glassy state, the distribution can be

envisioned to be more random, resulting in the probability of encountering shorter separations. The situation is similar to the one described some time ago for the glass-to-crystal transition in  $\text{CdGeP}_2$ .<sup>44</sup> This compound crystallizes in the chalcopyrite lattice, a zintl-type superstructure with P atoms strictly on anionic sites, whereas the glassy state can be envisioned in terms of a random close-packed structure, with a considerable probability of encountering other phosphorus atoms in the first coordination sphere. As a result, the average homonuclear  $^{31}\text{P}$ – $^{31}\text{P}$  dipolar coupling strength is significantly stronger in the glassy than in the crystalline state. We invoke an analogous explanation in the present system, where the random organization of coordination polyhedra may result in shorter  $^{31}\text{P}$ – $^{31}\text{P}$  distances not encountered in the crystals. The formation of P–O–P linkages appears unlikely, however, as no separate peaks for such  $\text{Q}^{(1)}$  species are observed.

**$^7\text{Li}$  MAS NMR.** The  $^7\text{Li}$  MAS NMR spectra in the glassy state were found to be Gaussian-shaped curves centered at  $-0.8$  ppm, with line widths of  $3300 \pm 100$  Hz.

**$^{27}\text{Al}$  Single and Double Resonance MAS NMR.** Figure 11 shows the  $^{27}\text{Al}$  MAS NMR spectra obtained for the present

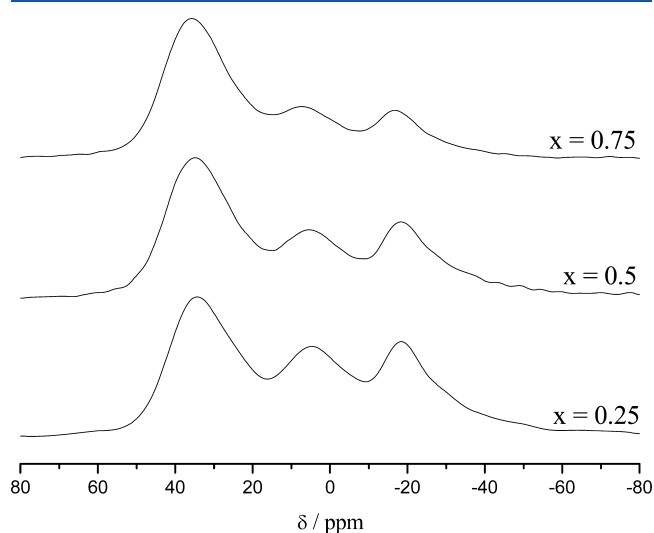


**Figure 11.**  $^{27}\text{Al}$  MAS NMR spectra of glassy  $\text{Li}_{1+x}\text{Al}_x\text{Ge}_{2-x}(\text{PO}_4)_3$  with three distinct compositions  $x$ .

glasses. They indicate the presence of four-, five-, and six-coordinated aluminum, similar to the situation in many alkali aluminophosphate glasses. As observed for these reference systems, there is a tendency toward increased concentrations of four-coordinate Al with increasing Al/P ratio. Table 4 summarizes the  $^{27}\text{Al}$  NMR interaction parameters for these different Al environments, as extracted from TQ MAS NMR data.

As the four-coordinate Al species are generally considered network forming species, the possibility of Al–O–Ge linkages (which are analogous to Al–O–Si linkages in aluminosilicate glasses) must be considered. This question can be explored on the basis of the  $^{27}\text{Al}\{^{31}\text{P}\}$  REDOR results shown in Figure 12. As is the case for the large majority of aluminophosphate glasses, the  $^{27}\text{Al}\{^{31}\text{P}\}$  REDOR curves obtained for the  $\text{Al}^{(4)}$ ,  $\text{Al}^{(5)}$ , and  $\text{Al}^{(6)}$  species are essentially indistinguishable within experimental error, suggesting comparable interaction strengths (see Figure S4, Supporting Information). For this reason, the REDOR difference signal was determined from the integrated

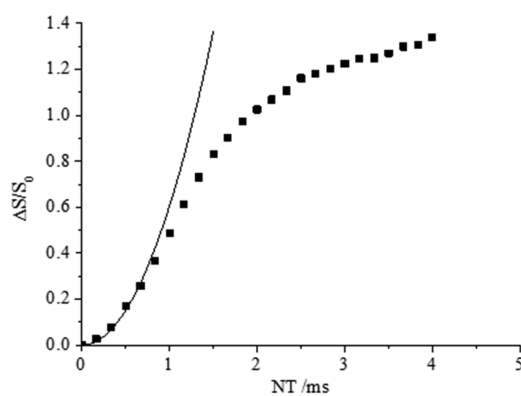


**Figure 12.**  $^{27}\text{Al}\{^{31}\text{P}\}$  compensated REDOR curve of glass with the nominal composition  $\text{Li}_{1.5}\text{Al}_{0.5}\text{Ge}_{1.5}(\text{PO}_4)_3$ . The solid curve is a parabolic fit to the experimental data points within the range  $\Delta S/S_0 < 0.3$ .

areas over the entire  $^{27}\text{Al}$  NMR line shape. The heteronuclear dipolar second moment value obtained in this manner,  $M_2^{\text{hetero}}$  near  $4.4 \times 10^6 \text{ rad}^2/\text{s}^2$ , is comparable to that measured for other aluminophosphate glasses<sup>45</sup> and strongly suggests that the second coordination sphere of the Al atoms is dominated by phosphorus atoms. We may thus conclude that Al–O–Ge linkages do not make a substantial contribution to the structures of these glasses.

This conclusion is confirmed independently by the  $^{27}\text{Al}\{^7\text{Li}\}$  REDOR data summarized in Figure 13. These data do not lend

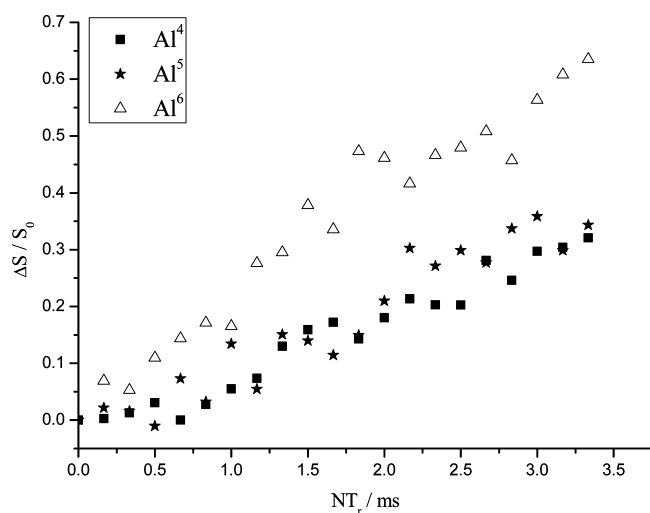


**Figure 13.**  $^{27}\text{Al}\{^7\text{Li}\}$  REDOR curves measured for the three distinct aluminum coordination states in a glass with the nominal composition  $\text{Li}_{1.5}\text{Al}_{0.5}\text{Ge}_{1.5}(\text{PO}_4)_3$ .

themselves to a quantitative analysis in terms of second moments because their evaluation is complicated by the fact that owing to the anisotropic  $^7\text{Li}$  nuclear electric quadrupolar interaction only a fraction of the  $^7\text{Li}$  nuclei in the outer Zeeman states will contribute to the dephasing of proximal  $^{27}\text{Al}$  nuclei. Nevertheless, they do show an interesting discrimination of Al coordination state with respect to the proximity of lithium: the  $\text{Al}^{(6)}$  species interact significantly more strongly with Li than the  $\text{Al}^{(5)}$  and the  $\text{Al}^{(4)}$  species. We may conclude from this result that the structural role of the four-coordinate aluminum species is likely to be rather different from the usual role of  $\text{Al}^{(4)}$

in aluminosilicate glasses (or aluminogermanate glasses, for that matter), where they represent anionic centers whose charge is being compensated by alkali ions. Here, it appears more likely that the local environment of the  $\text{Al}^{(4)}$  species resembles that in crystalline  $\text{AlPO}_4$ .

## CONCLUSIONS

In conclusion, multinuclear single and double resonance solid state NMR results indicate that the crystallization of glasses in the system  $\text{Li}_{1+x}\text{Al}_x\text{Ge}_{2-x}(\text{PO}_4)_3$  is associated with dramatic structural changes, in particular with regard to the coordination state of the aluminum and (by inference) the germanium species. Nevertheless, dipolar solid state NMR experiments indicate that the phosphate species in both phases are dominated by Ge–O–P and Al–O–P connectivities, while P–O–P and Ge–O–Al connectivities are largely absent. Crystalline materials with  $x < 0.5$  are best described as solid solutions with the NASICON structure, where Al and Ge are exclusively six-coordinated. Aliovalent substitution of germanium by aluminum in the crystalline phases results in an expansion of the  $\text{AlO}_6$  coordination polyhedra, as suggested by  $^{31}\text{P}\{^{27}\text{Al}\}$  REAPDOR results as well as by site resolved  $^{31}\text{P}$ -DQ DRENAR experiments. For samples with  $x \geq 0.5$ , glass crystallization is accompanied by the formation of some nanocrystalline  $\text{AlPO}_4$ , suggesting phase separation to some extent. This latter result explains why, according to several studies, the ionic conductivity of  $\text{Li}_{1+x}\text{Al}_x\text{Ge}_{2-x}(\text{PO}_4)_3$  glass ceramics does not increase significantly beyond  $x = 0.5$ , despite the expected linear increase of mobile ion carriers with increasing  $x$ . Samples with  $x > 0.5$  are multiphase, featuring lithium sequestration into  $\text{Li}_4\text{P}_2\text{O}_7$  and an additional non-conducting  $\text{AlPO}_4$  phase impeding long-range charge transport. Thus, solid state NMR is an extremely sensitive method for characterizing the stability range of the NASICON solid-solution system, allowing composition and ceramization conditions to be optimized for maximum yield of the superionic crystalline phase with the highest possible lithium content.

## ASSOCIATED CONTENT

### Supporting Information

S1, Differential scanning thermograms of the glassy samples; S2, X-ray powder diffraction pattern of the crystalline samples; S3,  $^{27}\text{Al}$ – $^{27}\text{Al}$  SQ/DQ correlation spectra of crystallized  $\text{Li}_{1.75}\text{Al}_{0.75}\text{Ge}_{1.25}(\text{PO}_4)_3$ ; S4,  $\{^{27}\text{Al}\}^{31}\text{P}$  CP/HETCOR results on crystallized  $\text{Li}_{1.5}\text{Al}_{0.5}\text{Ge}_{1.5}(\text{PO}_4)_3$ ; S5, site resolved  $^{27}\text{Al}\{^{31}\text{P}\}$  REDOR curves for the  $\text{Al}^{(4)}$ ,  $\text{Al}^{(5)}$ , and  $\text{Al}^{(6)}$  species in glassy  $\text{Li}_{1.5}\text{Al}_{0.5}\text{Ge}_{1.5}(\text{PO}_4)_3$ ; and S6,  $^{27}\text{Al}$  TQMAS-NMR spectrum of glassy  $\text{Li}_{1.5}\text{Al}_{0.5}\text{Ge}_{1.5}(\text{PO}_4)_3$  are included. This material is available free of charge via the Internet at <http://pubs.acs.org>.

## AUTHOR INFORMATION

### Corresponding Author

\*E-mail: [eckert@uni-muenster.de](mailto:eckert@uni-muenster.de); [eckert@ifsc.usp.br](mailto:eckert@ifsc.usp.br).

### Notes

The authors declare no competing financial interest.

## ACKNOWLEDGMENTS

Support by FAPESP (Sao Paulo Research Foundation), Grant No. 2013/07793-6 (CERTEV – Center for Research, Technology and Education in Vitreous Materials), is most gratefully acknowledged.

## REFERENCES

- (1) Scrosati, B.; Hassoun, J.; Sun, Y.-K. Lithium-Ion Batteries. A Look into the Future. *Energy Environ. Sci.* **2011**, *4*, 3287–3295.
- (2) Jiang, S. P.; Wang, X., Fuel Cells: Advances and Challenges, in Solid State Electrochemistry II: Electrodes, Interfaces and Ceramic Membranes, 1st ed.; Wiley-VCH Verlag GmbH & Co. KGaA: Weinheim, 2011; pp 179–264.
- (3) Malavasi, L.; Fisher, C. A. J.; Islam, M. S. Oxide-Ion and Proton Conducting Electrolyte Materials for Clean Energy Applications: Structural and Mechanistic Features. *Chem. Soc. Rev.* **2010**, *39*, 4370–4387.
- (4) Masquelier, C. Solid Electrolytes: Lithium ions on the Fast Track. *Nature Mater.* **2011**, *10*, 648–650.
- (5) Etacheri, V.; Marom, R.; Elazari, R.; Salitra, G.; Aurbach, D. Challenges in the Development of Advanced Li-Ion Batteries: A Review. *Energy Environ. Sci.* **2011**, *4*, 3243–3262.
- (6) Knauth, P. Inorganic Solid Li Ion Conductors: An Overview. *Solid State Ionics* **2009**, *180*, 911–916.
- (7) Minami, T.; Hayashi, A.; Tatsumisago, M. Recent Progress of Glass and Glass-Ceramics as Solid Electrolytes for Lithium Secondary Batteries. *Solid State Ionics* **2006**, *177*, 2715–2720.
- (8) Fergus, J. W. Ceramic and Polymeric Solid Electrolytes for Lithium-Ion Batteries. *J. Power Sources* **2010**, *195*, 4554–4569.
- (9) Xu, X. X.; Wen, Z. Y.; Gu, Z. H.; Xu, X. H.; Lin, Z. X. Lithium Ion Conductive Glass Ceramics in the System  $\text{Li}_{1-x}\text{Al}_x\text{Ge}_{1-x}\text{Ti}_x(\text{PO}_4)_3$  ( $x = 0-1.0$ ). *Solid State Ionics* **2004**, *171*, 207–213.
- (10) Narvarez-Semanate, J. L.; Rodrigues, A. C. M. Microstructure and Ionic Conductivity of  $\text{Li}_{1-x}\text{Al}_x\text{Ti}_{2-x}(\text{PO}_4)_3$  NASICON Glass-Ceramics. *Solid State Ionics* **2010**, *181*, 1197–1204.
- (11) Cruz, A. M.; Ferreira, E. B.; Rodrigues, A. C. M. Controlled Crystallization and Ionic Conductivity of a Nanostructured  $\text{LiAlGePO}_4$  Glass-Ceramic. *J. Non-Cryst. Solids* **2009**, *355*, 2295–2301.
- (12) Yamamoto, H.; Tabuchi, M.; Takeuchi, T.; Kageyama, H.; Nakamura, O. Ionic Conductivity Enhancement in  $\text{LiGe}_2(\text{PO}_4)_3$  Solid Electrolyte. *J. Power Sources* **1997**, *68*, 397–401.
- (13) Fu, J. Fast  $\text{Li}^+$  Ion Conducting Glass-Ceramics in the System  $\text{Li}_2\text{O}-\text{Al}_2\text{O}_3-\text{GeO}_2-\text{P}_2\text{O}_5$ . *Solid State Ionics* **1997**, *104*, 191–194.
- (14) Maldonado-Manso, P.; Losilla, E. R.; Martinez-Lara, M.; Aranda, M. A. G.; Bruque, S.; Mouahid, F. E.; Zahir, M. High Lithium Ionic Conductivity in the  $\text{Li}_{1-x}\text{Al}_x\text{Ge}_y\text{Ti}_{2-x-y}(\text{PO}_4)_3$  NASICON Series. *Chem. Mater.* **2003**, *15*, 1879–1885.
- (15) Aono, H.; Sugimoto, E.; Sadaoka, Y.; Imanaka, N.; Adachi, G.-Y. Ionic Conductivity of Solid Electrolytes Based on Lithium Titanium Phosphate. *J. Electrochem. Soc.* **1990**, *137*, 1023–1027.
- (16) Alami, M.; Brochu, R.; Soubeyroux, J. L.; Gravereau, P.; Le Flem, G.; Hagenmuller, P. Structure and Thermal Expansion of  $\text{LiGe}_2(\text{PO}_4)_3$ . *J. Solid State Chem.* **1991**, *90*, 185–193.
- (17) Shimonishi, Y.; Zhang, T.; Imanishi, N.; Im, D.; Lee, D. J.; Hirano, A.; Takeda, Y.; Yamamoto, O.; Sammes, N. A Study on Lithium/Air Secondary Batteries - Stability of the NASICON-Type Lithium Ion Conducting Solid Electrolyte in Alkaline Aqueous Solutions. *J. Power Sources* **2011**, *196*, 5128–5132.
- (18) Hasegawa, S.; Imanishi, N.; Zhang, T.; Xie, J.; Hirano, A.; Takeda, Y.; Yamamoto, O. Study on Lithium/Air Secondary Batteries-Stability of NASICON-Type Lithium Ion Conducting Glass-Ceramics with Water. *J. Power Sources* **2009**, *189*, 371–377.
- (19) Eckert, H. Short and Medium Range Order in Ion Conducting Glasses Studied by Modern Solid State NMR Techniques. *Z. Phys. Chem.* **2010**, *224*, 1591–1653.
- (20) Paris, M. A.; Sanz, J. Structural Changes in the compounds  $\text{LiM}_2(\text{PO}_4)_3$  ( $M = \text{Ge, Ti, Sn, and Hf}$ ) as Followed by  $^{31}\text{P}$  and  $^7\text{Li}$  NMR. *Phys. Rev. B* **1997**, *55*, 14270–14278.
- (21) Arbi, K.; Mandal, S.; Rojo, J. M.; Sanz, J. Dependence of Ionic Conductivity on Composition of Fast Ionic Conductors  $\text{Li}_{1-x}\text{Ti}_{2-x}\text{Al}_x(\text{PO}_4)_3$  ( $0 < x < 0.7$ ). A Parallel NMR and Electric Impedance Study. *Chem. Mater.* **2002**, *14*, 1091–1097.
- (22) Wong, S.; Newman, P. J.; Best, A. S.; Nairn, K. M.; Macfarlane, D. R.; Forsyth, M. Towards Elucidating Microscopic Structural Changes in Li Ion Conductors  $\text{Li}_{1+y}\text{Ti}_{2-y}\text{Al}_y(\text{PO}_4)_3$  and  $\text{Li}_{1+y}\text{Ti}_{2-y}\text{Al}_y(\text{PO}_4)_{3-x}(\text{MO}_4)_x$  ( $M = \text{V and Nb}$ ): X-ray and  $^{27}\text{Al}$  and  $^{31}\text{P}$  NMR Studies. *J. Mater. Chem.* **1998**, *8*, 2199–2203.
- (23) Forsyth, M.; Wong, S.; Naim, K. M.; Best, A. S.; Newman, P. J.; MacFarlane, D. R. NMR Studies of Modified NASICON-Like Lithium Ion Solid Electrolytes. *Solid State Ionics* **1999**, *124*, 213–219.
- (24) Maldonado-Manso, P.; Martin-Sedeno, M. C.; Bruque, S.; Sanz, J.; Losilla, E. R. Unexpected Cationic Distribution in Tetrahedral/Octahedral Sites in Nominal  $\text{Li}_{1+x}\text{Al}_x\text{Ge}_{2-x}(\text{PO}_4)_3$  NASICON Series. *Solid State Ionics* **2007**, *178*, 43–52.
- (25) Arbi, K.; Paris, M. A.; Sanz, J. Li Mobility in Nasicon Type Materials  $\text{LiM}_2(\text{PO}_4)_3$ ,  $M = \text{Ge, Ti, Sn, Zr, and Hf}$ , Followed by  $^7\text{Li}$  NMR Spectroscopy. *Dalton Trans.* **2011**, *40*, 10195–10202.
- (26) Arbi, K.; Tabellout, M.; Lazarraga, M. G.; Rojo, J. M.; Sanz, J. Non-Arrhenius Conductivity in the Fast Lithium Conductor  $\text{Li}_{1.2}\text{Ti}_{1.8}\text{Al}_{0.2}(\text{PO}_4)_3$ : A  $^7\text{Li}$  NMR and Electric Impedance Study. *Phys. Rev. B* **2005**, *72*, 094302.
- (27) Gullion, T.; Schaefer, J. Rotational Echo Double Resonance NMR. *J. Magn. Reson.* **1989**, *81*, 196–201.
- (28) Chan, J. C. C.; Eckert, H. Dipolar Coupling Information in Multi-Spin Systems: Application of a Compensated REDOR NMR Approach to Inorganic Phosphates. *J. Magn. Reson.* **2000**, *147*, 170–178.
- (29) Bertmer, M.; Eckert, H. Dephasing of Spin Echoes by Multiple Dipolar Interactions in Rotational Echo Double Resonance NMR Experiments. *Solid State Nucl. Magn. Reson.* **1999**, *15*, 139–152.
- (30) van Vleck, J. H. The Dipolar Broadening of Magnetic Resonance Lines in Crystals. *Phys. Rev.* **1948**, *74*, 1168–1183.
- (31) Gullion, T.; Vega, A. Measuring Heteronuclear Dipolar Couplings for  $I = 1/2$ ,  $S > 1/2$  Spin Pairs by REDOR and REAPDOR NMR. *Prog. Nucl. Magn. Reson. Spectrosc.* **2005**, *47*, 123–126.
- (32) Medek, A.; Harwood, J. S.; Frydman, L. Multiple-Quantum Magic-Angle Spinning NMR: A New Method for the Study of Quadrupolar Nuclei in Solids. *J. Am. Chem. Soc.* **1995**, *117*, 12779–12787.
- (33) Amoureux, J. P.; Fernandez, C.; Steuernagel, S. Z Filtering in MQMAS NMR. *J. Magn. Reson.* **1996**, *A123*, 116–118.
- (34) Edén, M.; Zhou, D.; Yu, J. Improved Double-quantum NMR Correlation Spectroscopy of Dipolar-coupled Quadrupolar Spins. *Chem. Phys. Lett.* **2006**, *431*, 397–403 and references therein.
- (35) Wang, Q.; Hu, B.; Lafon, O.; Trebosc, J.; Deng, F.; Amoureux, J. P. Double Quantum Homonuclear Correlation Spectroscopy of Quadrupolar Nuclei Subjected to Magic-Angle Spinning and High Magnetic Field. *J. Magn. Reson.* **2009**, *200*, 251–260.
- (36) Ren, J.; Eckert, H. DQ-DRENAR: A New NMR Technique to Measure Site-Resolved Magnetic Dipole-Dipole Interactions in Multispin-1/2 Systems. Theory and Applications to Phosphate Materials. *J. Chem. Phys.* **2013**, *138*, 164201/1–16.
- (37) Hohwy, M.; Jakobsen, H. J.; Edén, M.; Levitt, M. H.; Nielsen, N. C. Broadband Dipolar Recoupling in the Nuclear Magnetic Resonance of Rotating Solids: A Compensated C7 Pulse Sequence. *J. Chem. Phys.* **1998**, *108*, 2686–2694.
- (38) Losilla, E. R.; Aranda, M. A. G.; Bruque, S.; Sanz, J.; Paris, M. A.; Campo, J.; West, A. R. Sodium Mobility in the NASICON Series  $\text{Na}_{1+x}\text{Zr}_{2-x}\text{In}_x(\text{PO}_4)_3$ . *Chem. Mater.* **2000**, *12*, 2134–2142.
- (39) Bak, M.; Rasmussen, J. T.; Nielsen, N. C. SIMPSON: A General Simulation Program for Solid-State NMR Spectroscopy. *J. Magn. Reson.* **2000**, *147*, 296–330.
- (40) Lo, A.; Edén, M. Efficient Symmetry-based Homonuclear Dipolar Recoupling of Quadrupolar Spins: Double-quantum NMR Correlations in Amorphous Solids. *Phys. Chem. Chem. Phys.* **2008**, *10*, 6635–6644.
- (41) Eckert, H.; Zhang, Z.; Kennedy, J. H. Solid State NMR Studies of Ionically Conductive Non-Oxide Chalcogenide Glasses. *Mater. Res. Soc. Symp. Proc.* **1989**, *135*, 259–264.
- (42) Dupree, R.; Holland, D.; Mortuza, M. G.; Collins, J. A.; Lockyer, M. W. G. Magic-Angle Spinning NMR of Alkali Phospho Alumina Silicate Glasses. *J. Non-Cryst. Solids* **1989**, *112*, 111–119.



(43) van Wüllen, L.; Gee, B.; Züchner, L.; Bertmer, M.; Eckert, H. Connectivities and Cation Distributions in Oxide Glasses: New Results from Solid State NMR. *Ber. Bunsen-Ges.* **1996**, *100*, 1539–1549.

(44) Franke, D.; Maxwell, R.; Lathrop, D.; Eckert, H. Structural Models for Covalent Non-Oxidic Glasses. Atomic Distribution and Local Order in Glassy  $\text{CdGeP}_2$  Studied by  $^{31}\text{P}$  and  $^{113}\text{Cd}$  MAS, Spin Echo, and  $^{31}\text{P}$ - $^{113}\text{Cd}$  Spin Echo Double Resonance NMR Spectroscopy. *J. Am. Chem. Soc.* **1991**, *113*, 4822–4830.

(45) Zhang, L.; Eckert, H. Short- and Medium-Range Order in Sodium Aluminophosphate Glasses: New Insights from High-Resolution Dipolar Solid State NMR Spectroscopy. *J. Phys. Chem. B* **2006**, *110*, 8946–8958.